Bull Math Biol (2011) 73:3071–3089
DOI 10.1007/s11538-011-9661-5

ORIGINAL ARTICLE

Empirical Study of an Adaptive Multiscale Model for Simulating Cardiac Conduction

Paul E. Hand · Boyce E. Griffith

Received: 19 August 2010 / Accepted: 8 April 2011 / Published online: 30 April 2011

Abstract We modify and empirically study an adaptive multiscale model for simulating cardiac action potential propagation along a strand of cardiomyocytes. The model involves microscale partial differential equations posed over cells near the action potential upstroke and macroscale partial differential equations posed over the remainder of the tissue. An important advantage of the modified model of this paper is that, unlike our original model, it does not require perfect alignment between myocytes and the macroscale computational grid. We study the effects of gap-junctional coupling, ephaptic coupling, and macroscale grid spacing on the accuracy of the multiscale model. Our simulations reveal that the multiscale method accurately reproduces both the wavespeed and the waveform, including both upstroke and recovery, of fully microscale models. They also reveal that perfect alignment between myocytes and the macroscale grid is not necessary to reproduce the dynamics of a traveling action potential. Further, our simulations suggest that the macroscale grid spacing used in an adaptive multiscale model need not be much finer than the spatial width of an action potential. These results are demonstrated to hold under high, low, and zero gap-junctional coupling regimes.

Keywords Ephaptic · Multiscale · Adaptive · Cardiac modeling · Gap junction

1 Introduction

Computer simulations of the heart have the potential to improve our understanding of normal and pathological cardiac dynamics and promise to accelerate the development

P.E. Hand (✉) · B.E. Griffith
Leon H. Charney Division of Cardiology, New York University School of Medicine, New York, NY 10016, USA
e-mail: hand@cims.nyu.edu

of new medical therapies. To fulfill this promise in the context of whole-heart simulations, it is necessary to use computationally tractable models of heart tissue that accurately capture action potential dynamics. The most natural descriptions of cardiac electrophysiology fall into two classes: those that are fully microscopic, in which individual cells are explicitly resolved, and those that are fully macroscopic, in which the details of individual cells are averaged away and the tissue is only considered in bulk. Each class of models has its benefits and disadvantages.

The primary difficulty with fully microscale models is that they are too computationally expensive to scale up to whole-heart simulations. As an illustration, consider a slab of ventricular muscle with dimensions $10\,\text{cm} \times 10\,\text{cm} \times 1\,\text{cm}$, roughly the dimensions of the wall of the ventricular myocardium of a human heart. If a typical cardiomyocyte is of dimensions $10^{-2}\,\text{cm} \times 10^{-3}\,\text{cm} \times 10^{-3}\,\text{cm}$ (Keener and Sneyd 1998), this slab contains $O(10^{10})$ myocytes. Were each cell to be resolved by ten nodes and supplemented with tens of state variables per node, there would be $O(10^{12})$ degrees of freedom. Hence, whereas the biophysics is most accurately and naturally posed at the microscale, the tremendous computational resources required by such models imply that whole-heart simulations cannot be exclusively based on microscale models. Moreover, because most of the nontrivial dynamics in ventricular myocytes occur only in the vicinity of sharp action potential wavefronts, even if such fully microscale whole-heart models were computationally feasible, they would likely be unnecessarily computationally intensive.

Fully macroscale simulations are much less computationally expensive than fully microscale ones; however, they may still be quite demanding, especially for grids of fixed spacing. Indeed, action potential upstrokes can have widths of a couple hundred microns (Boron and Boulpaep 2005). Hence, a fixed-size mesh does not yield accurate results at spacings much coarser than approximately 200 μm. At such resolutions, Bordas et al. (2009) estimate that it would take six weeks to run a 1-second simulation on 64 processors of a modern supercomputer, even with a simplistic ionic current model and generous assumptions on algorithmic performance. The expense of even fully macroscale simulations with uniform mesh sizes suggests that adaptive methods may be required. For example, Cherry et al. (2000, 2003) and Colli Franzone et al. (2006) use adaptive macroscale methods to gain about two orders of magnitude in computational speed when compared to corresponding uniformly fine fixed-mesh simulations.

A further difficulty with fully macroscale simulations is that they can be inaccurate under low levels of gap-junctional (GJ) coupling, even if the simulations are highly resolved or use adaptive mesh spacing. As observed in Hand and Griffith (2010), for such cases, fully macroscale simulations are extremely sensitive to the spacing of the computational grid. Specifically, macroscale simulations can incorrectly predict conduction block if grid spacing is too large, and they can also fail to predict conduction block if grid spacing is too small. Such errors are not surprising because the derivation of the macroscale equations assumes electrical potential and gating variables vary slowly over the length scale of cells (Neu and Krassowska 1993; Hand et al. 2009). This assumption is strongly violated under low gap-junctional coupling because, in such cases, action potential upstrokes may be only a single cell wide (Hand and Griffith 2010).

The pathophysiological regime of low gap-junctional coupling is important because downregulation of gap-junction expression can occur in various types of cardiac disease (Severs et al. 2004), such as in cardiac ischemia or hypertrophy, or in the infarct border zone (Smith et al. 1991; Peters et al. 1993; Severs et al. 2008). Such gap-junctional remodeling is associated with arrhythmogenesis and may lead to sudden cardiac death resulting from ventricular fibrillation (Gutstein et al. 2001). To study how alterations in expression of connexin43 (Cx43), the major ventricular gap-junction protein, affect cardiac conduction, Gutstein et al. (2001) performed a gene-knockout study that demonstrated that Cx43-deficient mice exhibit cardiac conduction, albeit at slower speeds than usual. They also did not find a compensatory increase in the expression of other connexin isoforms (Gutstein et al. 2001). Further, in a subsequent study, they also found that gap-junctional coupling was essentially abolished in isolated cell pairs extracted for Cx43-null ventricular tissue (Yao et al. 2003). These findings are surprising because gap junctions are generally accepted as the primary mechanism of normal cardiac electrical communication (Rohr 2004), and they suggest that there are important electrical coupling mechanisms in cardiac tissue besides gap-junctionally mediated coupling (Sperelakis and Mann 1977; Picone et al. 1991; Ramasamy and Sperelakis 2007; Mori et al. 2008; Copene and Keener 2008; Hand and Peskin 2010; Hand and Griffith 2010; Lin and Keener 2010).

One candidate biophysical mechanism is known as ephaptic coupling or as the electric-field mechanism. In it, adjacent cells interact through a narrow shared cleft space located at the intercalated discs. When one cell's cleft-facing Na^+ channels open, current flows into the "prejunctional" cell via the cleft, thereby reducing the cleft potential relative to the extracellular bulk. This drop in extracellular potential increases the transmembrane potential difference across the cleft-facing membrane of the opposing "postjunctional" cell. In some cases, this depolarization is sufficient to excite the postjunctional cell, thereby continuing the propagation of the electrical signal. Low gap-junctional simulations, with and without ephaptic coupling, may be helpful in understanding the experimental observations of Gutstein et al. (2001) and may ultimately help to design or to optimize therapies for patients with gap-junctional remodeling.

We believe that it is necessary to use a multiscale approach to make efficient simulations of cardiac conduction at the organ scale under low levels of gap-junctional coupling. That is, such simulations should deploy a microscale, cell-level model near sharp action potential wavefronts, and a macroscale, tissue-level description of cardiac muscle away from such wavefronts. We have previously introduced such a multiscale model for a one-dimensional fiber of cells, both with and without ephaptic coupling (Hand and Griffith 2010). This adaptive multiscale method has been shown to capture accurately the action potential upstroke and wavespeed over a wide range of nonzero gap-junctional coupling levels. However, our earlier work did not study whether recovery was also accurately captured, nor whether the results held in the absence of gap junctions. It also did not study whether macroscale grid spacing could be coarse enough to greatly reduce overall computational cost of three-dimensional simulations. Finally, the interface conditions used in this earlier model required the myocytes to be perfectly aligned with the macroscopic grid, so that the ends of any macroscale computational control volume coincided with the ends of microscopic

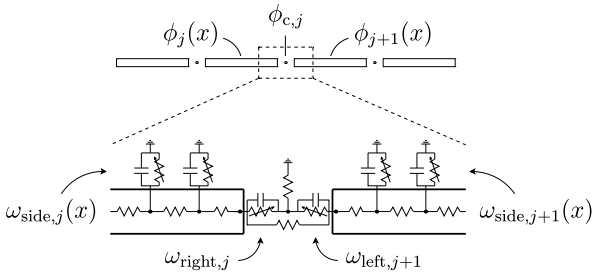

Fig. 1 The microscale geometry and equivalent circuit of our model of a strand of cardiomyocytes. Notice that adjacent cells are coupled directly through a resistor, which represents gap-junctional connections, and through a shared cleft space at the intercalated discs. In the figure, cleft spaces are depicted as having nonzero width; however, in the model, these spaces, which are on the order of tens to hundreds of nanometers (Kucera et al. 2002), are idealized as having zero width. Figure adapted from Hand and Griffith (2010)

myocytes. This requirement makes generalizing the interface conditions to three dimensions difficult because fiber rotation guarantees the interface between micro- and macroscale descriptions will not generally coincide with the ends of cells.

In the present paper, we modify the interface conditions of the multiscale method of Hand and Griffith (2010). In essence, the new conditions focus on balancing cytosolic current, whereas the old interface conditions focused on balancing gap-junctional current. We perform simulations to demonstrate that the modified model is able to capture accurately both the upstroke and the downstroke of the cardiac action potential, is applicable to the purely ephaptic parameter regime, and is relatively insensitive to the grid spacing employed to simulate the macroscopic part of the tissue.

2 Multiscale Model

We consider a linear fiber of length L composed of cylindrical cardiomyocytes, each of length ℓ and radius r. Adjacent cells are coupled by resistive connections, representing gap junctions, and possibly by an ephaptic mechanism via a shared cleft that is resistively connected to grounded extracellular space. In the case in which the cleft-to-ground resistance is zero, there is no ephaptic coupling. Figure 1 provides a schematic depiction of the cell-scale model and its discretization.

The adaptive multiscale method works as follows. Given a voltage profile across the strand of myocytes, adaptivity criteria described below determine which spatial regions should be described by an low-resolution macroscale model, and which regions should be described by a high-resolution microscale model; see Fig. 2. Borrowing terminology from adaptive mesh refinement methods for partial differential equations (PDEs), we call the boundary between the regions of low resolution and high resolution the coarse-fine interface. At such interfaces, the macroscale and microscale PDE systems are coupled via interface conditions described below. As depicted in Fig. 2, the coarse-fine interface can occur at any point along the interior of a cell. We call myocytes in the high- or low-resolution regions resolved or unresolved, respectively.

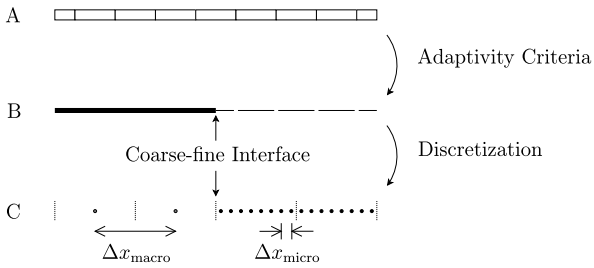

Fig. 2 A depiction of the strand of myocytes that underlie our model (**A**), a possible multiscale representation (**B**), and its corresponding spatial discretization (**C**). Given the potential over the entire domain, the adaptivity criteria (12)–(13) select which myocytes are to be resolved. We require the myocytes in each interval of width Δx_{macro} to be either all resolved or all unresolved. Note that the coarse-fine interface intersects the interior of a cell. In (**C**), each resolved myocyte is depicted with four interior nodes per full length cell. Boundary nodes at the intercalated discs of resolved myocytes are omitted for clarity. Figure adapted from Hand and Griffith (2010)

2.1 Microscale System

We consider the PDE analogue of the microscale model of Kucera et al. (2002), as we have done previously (Hand and Griffith 2010). Let $\phi_j = \phi_j(x,t)$ be the intracellular potential inside the jth cell, with $0 \le x \le \ell$. Let $\phi_{\text{c},j} = \phi_{\text{c},j}(t)$ be the potential in the cleft to the right of the jth cell. Let $\omega_{\text{left},j} = \omega_{\text{left},j}(t)$, $\omega_{\text{side},j} = \omega_{\text{side},j}(x,t)$, and $\omega_{\text{right},j} = \omega_{\text{right},j}(t)$ be the gating variables along the left end, the side, and the right end of the jth cell, respectively. The microscale system of PDEs posed over the resolved cells is given by:

$$C\partial_t \phi_j = \frac{A}{S}\sigma_{\text{cyt}}\partial_{xx}\phi_j - I_{\text{ion,side}}(\phi_j, \omega_{\text{side},j}), \tag{1}$$

$$\begin{aligned} C\partial_t\big(\phi_j(0,t) - \phi_{\text{c},j-1}\big) &= \sigma_{\text{cyt}}\partial_x\phi_j(0,t) - g_{\text{GJ}}\big(\phi_j(0,t) - \phi_{j-1}(\ell,t)\big) \\ &\quad - I_{\text{ion,end}}\big(\phi_j(0,t) - \phi_{\text{c},j-1}, \omega_{\text{left},j}\big), \end{aligned} \tag{2}$$

$$\begin{aligned} C\partial_t\big(\phi_j(\ell,t) - \phi_{\text{c},j}\big) &= -\sigma_{\text{cyt}}\partial_x\phi_j(\ell,t) - g_{\text{GJ}}\big(\phi_j(\ell,t) - \phi_{j+1}(0,t)\big) \\ &\quad - I_{\text{ion,end}}\big(\phi_j(\ell,t) - \phi_{\text{c},j}, \omega_{\text{right},j}\big), \end{aligned} \tag{3}$$

$$\phi_{\text{c},j} = \sigma_{\text{cyt}} R_{\text{c}} A\big(-\partial_x\phi_j(\ell,t) + \partial_x\phi_{j+1}(0,t)\big), \tag{4}$$

$$\partial_t\omega_{\text{side},j} = g(\phi_j, \omega_{\text{side},j}), \tag{5}$$

$$\partial_t\omega_{\text{left},j} = g\big(\phi_j(0,t) - \phi_{\text{c},j-1}, \omega_{\text{left},j}\big), \tag{6}$$

$$\partial_t\omega_{\text{right},j} = g\big(\phi_j(\ell,t) - \phi_{\text{c},j}, \omega_{\text{right},j}\big). \tag{7}$$

Here, $A = \pi r^2$ is the area of a cell's cross-section (cm^2), $S = 2\pi r$ is the perimeter of a cross-section (cm), σ_{cyt} is the cytosolic conductivity (mS/cm), g_{GJ} is the gap-junctional conductance per unit area (mS/cm^2) at the ends of cells, C is the membrane capacitance per unit area ($\mu\text{F/cm}^2$), R_{c} is the cleft-to-ground resistance ($\text{k}\Omega$), $I_{\text{ion,side}}$ and $I_{\text{ion,end}}$ are the ionic current densities ($\mu\text{A/cm}^2$) flowing out of

the side and end membranes of cells, and g represents the gating variable dynamics (1/ms). We distinguish between $I_{\text{ion,side}}$ and $I_{\text{ion,end}}$ because successful ephaptic conduction requires preferential localization of Na^+ channels to the intercalated discs. Such nonuniformity is biophysically motivated by the microhistological study of Kucera et al. (2002).

We comment that (2)–(4) can be combined to obtain an equation for the potential in a particular cleft in terms of the ionic and capacitive current flowing into that cleft.

2.2 Macroscale System

Let $\phi = \phi(x,t)$ be the intracellular potential of cells near x, with x denoting any point along the linear fiber. Similarly, let $\omega = \omega(x,t)$ be the gating variables of the side and ends of cells near x. Notice that this interpretation of ϕ and ω only makes sense if potential and gating variables are slowly varying over the length scale of cells. The macroscale system applied over the region of unresolved cells is given by

$$C\partial_t\phi = \frac{1}{S\ell + 2A}\ell\partial_x\left(A\sigma_{\text{cyt}}\left(1 - \frac{1}{1+\kappa}\right)\partial_x\phi\right) - I_{\text{ion}}(\phi,\omega), \tag{8}$$

$$\partial_t\omega = g(\phi,\omega). \tag{9}$$

Here, $\kappa = \ell g_{\text{GJ}}/\sigma_{\text{cyt}}$ is a nondimensional parameter comparing gap-junctional and cytosolic conductances. The gating variables at the sides and ends of the cells are not distinguished by this macroscale model and are therefore treated as equal.

Notice that R_c does not enter into (8)–(9). Although it is possible to derive macroscale equations that explicitly include ephaptic coupling (Hand and Peskin 2010), away from action potential upstrokes, there is very little Na^+ current flowing through clefts. Thus, the clefts have negligible potential, and the nonephaptic macroscale equations (8)–(9) are accurate (Hand and Griffith 2010). Both the epahptic and nonephaptic macroscale equations can be derived from macroscopic first principles or by the mathematical technique of homogenization (Keener and Sneyd 1998; Hand and Peskin 2010).

2.3 Interface Conditions

In our modified multiscale model, the microscale and macroscale descriptions are coupled exclusively through intracellular potential and cytosolic current. Let x^* be a point at the coarse-fine interface. Let j^* be the index of the fractional myocyte on the high-resolution side of the boundary. For convenience, we identify the domain of ϕ_{j^*} with the cell's actual spatial positions. Equations (1)–(9) are supplemented with the interface boundary conditions

$$\phi(x^*,t) = \phi_{j^*}(x^*,t), \tag{10}$$

$$-A\sigma_{\text{cyt}}\left(1 - \frac{1}{1+\kappa}\right)\partial_x\phi(x^*,t) = -A\sigma_{\text{cyt}}\partial_x\phi_{j^*}(x^*,t). \tag{11}$$

These interface conditions impose continuity of intracellular potential and cytosolic current at coarse-fine interfaces.

The coupling approach used in the original model of Hand and Griffith (2010) describes current between the microscale and macroscale exclusively in terms of gap-junctional current. As such current is only defined at the ends of myocytes, the model requires the macroscale grid to coincide with them. This requirement presents a significant barrier for extensions to realistic two- and three-dimensional simulations, in which fiber rotation will prevent any such coincidence. The present modification to the model therefore represents an important step toward such extensions, as it allows the macroscale grid to be unconstrained by the location of individual myocytes.

2.4 Adaptivity Criteria

Adaptivity criteria are used to determine which myocytes are to be resolved and which are to be left unresolved. Our "feature-detection" criteria attempt to use the higher resolution only near the action potential upstroke. The entire fiber length L is broken into computational volumes of the macroscale grid spacing Δx_{macro}, as depicted in Fig. 2C. A given macroscale computational volume is highly resolved if, at any point inside that volume,

$$\phi \geq -60 \text{ mV}, \quad \text{and} \tag{12}$$

$$\partial_t \phi \geq 0.1 \text{ mV/ms}. \tag{13}$$

Additionally, because action potential wavefronts travel from left to right in our simulations, the region of resolved cells is padded by a macroscale volume to the right of all volumes identified for refinement by (12)–(13). Whenever a macroscale computational volume is designated for refinement, it is left refined for a time of at least 1 ms. All other computational volumes are left at low resolution. These criteria are different than those in Hand and Griffith (2010). The present ones more naturally select the upstroke by basing selection on time derivatives, as opposed to space derivatives.

When a low-resolution region is selected to become high-resolution, potential and gating variables are prolonged onto the new grid points by constant prolongation. When a high-resolution region is selected to be low-resolution, the values are restricted onto the macroscale node by simple averaging.

3 Discretization

We assume the length of the macroscale and microscale regions to be integer multiples of the macroscale grid spacing Δx_{macro}. Resolved myocytes are broken into an integer number of nodes of spacing Δx_{micro}, which are half-offset from the cell boundaries. They also contain a node at each cell boundary that is entirely contained within the high-resolution region. Note that resolved cells may have different numbers of interior nodes because a coarse-fine interface can, in principle, intersect them at any point inside. We only require that the interface intersect a cell at a multiple of Δx_{micro} from the cell's ends. See Appendix A for the detailed discretization of the

PDEs (1)–(11). In our simulations, we used a time step of $\Delta t = 5 \cdot 10^{-4}$ ms for both the microscale and macroscale regions.

4 Numerical Results

We performed several collections of simulations using the adaptive multiscale model and its corresponding fully microscale analogue. In all cases, we considered a fiber of length $L = 10$ cm composed primarily of identical cells with radius $r = 11 \cdot 10^{-4}$ cm and length $\ell = 10^{-2}$ cm. As depicted in Fig. 2, the leftmost and rightmost cells in our model are "half cells" of length $\ell/2$. Because we will choose the macroscale spacing to be an integer multiple of the cell width, the coarse-fine interface always falls at the midpoint of resolved cells. See Table 1 for a full list of numerical values for the model parameters. In these simulations, we used the Fenton–Karma simplification of the Luo–Rudy model (Fenton and Karma 1998). We allow preferential excitability of end membranes by scaling the fast inward current in accordance with a given fraction f_{Na} of Na^+ channels expressed on the ends of cells. That is,

$$I_{\mathrm{ion,side}}(\phi, \omega) = (1 - f_{\mathrm{Na}})(1 + 2\alpha) I_{\mathrm{fi}}(\phi, \omega) + I_{\mathrm{si}}(\phi, \omega) + I_{\mathrm{so}}(\phi, \omega), \tag{14}$$

$$I_{\mathrm{ion,end}}(\phi, \omega) = f_{\mathrm{Na}} \frac{1 + 2\alpha}{2\alpha} I_{\mathrm{fi}}(\phi, \omega) + I_{\mathrm{si}}(\phi, \omega) + I_{\mathrm{so}}(\phi, \omega), \tag{15}$$

with $\alpha = \frac{A}{S\ell}$ and with I_{fi}, I_{so}, and I_{si} denoting the fast inward, the slow inward, and the slow outward currents of the Fenton–Karma model. Nonephaptic simulations have uniform Na^+ channel density, with $f_{\mathrm{Na}} = \frac{2\alpha}{1+2\alpha}$, whereas ephaptic simulations have $f_{\mathrm{Na}} = 1$, as in Kucera et al. (2002). Note that the Fenton–Karma Luo–Rudy model is a simplified ionic current model and does not, for example, explicitly describe Ca^{2+} current.

Initial conditions were set such that the leftmost region of width $10 \cdot \ell$ had potential 0 mV. As required by (4), all clefts were thus at 0 mV, and all gating variables and the remaining potential variables were at resting values. Note that only half of the 11th cell is initially excited because the leftmost cell has width $\ell/2$.

We define the location of a wavefront as the position where ϕ crosses -20 mV with $\partial_t \phi > 0$. We define the location of recovery for the wave as the position where ϕ crosses -20 mV with $\partial_t \phi < 0$. The speed of the activation wavefront and recovery waveback were computed by linear regression.

We performed four sets of simulations. Each set of simulations included both a fully microscale case, in which all cells were resolved, and a multiscale case, in which only the regions selected by the adaptivity criteria were subject to the high-resolution microscale model. In each case, the microscale grid spacing was $\Delta x_{\mathrm{micro}} = 2.5 \cdot 10^{-3}$ cm, whereas the macroscale grid spacing ranged from $\Delta x_{\mathrm{macro}} = 2 \cdot 10^{-2}$ cm to $\Delta x_{\mathrm{macro}} = 100 \cdot 10^{-2}$ cm. We assess the accuracy of the multiscale simulations by comparing them to results obtained from the fully microscale model.

The first set of simulations was meant to study the accuracy of the multiscale model in the high gap-junctional coupling regime in the absence of ephaptic coupling. In these simulations, g_{GJ} was set at its nominal level of 666 mS/cm^{-2} (Kucera et al. 2002); f_{Na} was set so that the Na^+ channel density is uniform, i.e., $f_{\mathrm{Na}} = \frac{2\alpha}{1+2\alpha}$, and $R_{\mathrm{c}} = 0$. The second set of simulations was meant to study the accuracy of the multiscale model in the low gap-junctional coupling regime but in the absence of ephaptic coupling. In these simulations, we took $g_{\mathrm{GJ}} = 6.66$ mS/cm^{-2}, which is 1% of its normal value, and set $R_{\mathrm{c}} = 0$. The third set of simulations was similar to the second set, except that it included ephaptic coupling by setting $R_{\mathrm{c}} = 8000$ kΩ and $f_{\mathrm{Na}} = 1$. The final set of simulations was meant to examine the accuracy of the multiscale model in the purely ephaptic regime, for which $g_{\mathrm{GJ}} = 0$ mS/cm^{-2}. Again, we chose $R_{\mathrm{c}} = 8000$ kΩ and $f_{\mathrm{Na}} = 1$. We remark that in the case of purely ephaptic conduction, in which there are no gap junctions, cells are coupled to neighbors only in the highly resolved region of the multiscale model. Everywhere else, the dynamics of the tissue are determined by spatially decoupled systems of ordinary differential equations.

The choice of $R_{\mathrm{c}} = 8000$ kΩ was made because preliminary simulations (not shown) revealed it to maximize approximately conduction speed in the low gap-junctional, ephaptic case. Cleft-to-ground resistance can be related to cleft width through the formula $R_{\mathrm{c}} = 1/8\pi\sigma_{\mathrm{ext}} w_{\mathrm{cleft}}$, in which σ_{ext} is the extracellular conductivity (mS/cm), and w_{cleft} is the cleft width (cm) (Kucera et al. 2002). Taking $\sigma_{\mathrm{ext}} = 6.67$ mS/cm (Kucera et al. 2002), this formula implies that $R_{\mathrm{c}} = 8000$ kΩ corresponds to $w_{\mathrm{cleft}} = 7$ nm. This relationship between R_{c} and w_{cleft} does not account for the tortuosity of the cleft. Were it to do so, the corresponding w_{cleft} value would necessarily be larger.

Figures 3–6 show the activation wavefronts and recovery wavebacks for all four sets of multiscale and macroscale simulations: high gap-junctional coupling in the absence ephaptic coupling, low gap-junctional coupling in the absence of ephaptic coupling, low gap-junctional coupling in the presence of ephaptic coupling, and purely ephaptic coupling in the absence of gap-junctional coupling. For all sets of simulations, the action potential upstrokes of the adaptive multiscale model agree with those of the underlying fully microscale models, even with $\Delta x_{\mathrm{macro}}$ as large as 1 cm. Note that all simulations localize the high-resolution region exclusively within a few multiples of $\Delta x_{\mathrm{macro}}$ around the upstroke. The accuracy of the simulations with $\Delta x_{\mathrm{macro}} = 0.5$ cm and 1 cm is seen to be parameter dependent. Specifically, these values of $\Delta x_{\mathrm{macro}}$ are most accurate in the high gap-junctional regime, for which the length scale of the action potential downstroke is quite large. They are least accurate in the low gap-junctional, nonephaptic case, in which the waveform is only a few multiples of $\Delta x_{\mathrm{macro}}$. In the case of high gap-junctional coupling, observe that the wave is much broader than the domain size. Nonetheless, the recovery phase is accurately computed by the adaptive multiscale model. Figure 7 shows how the wavefront speeds, waveback speeds, and spatial extent between upstroke and downstroke depend on the value of $\Delta x_{\mathrm{macro}}$. All three of these quantities are mostly constant over the broad range of $\Delta x_{\mathrm{macro}}$ surveyed, indicating that macroscale grid spacings of up to 1 cm may be used without substantially affecting the accuracy of the multiscale model.

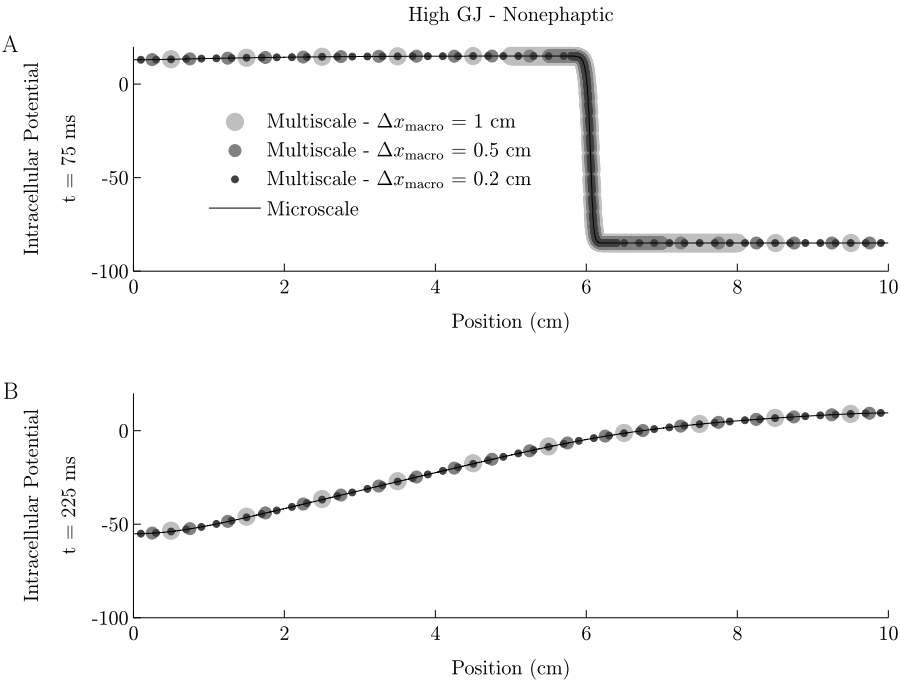

Fig. 3 The intracellular potential at two different times for the high gap-junctional, nonephaptic simulations with varying macroscale grid spacing. Panel **A** shows an upstroke, and panel **B** shows a recovery. Note that myocytes are resolved only near the upstroke, which can be seen by the blur of gray circular marks. In these simulations, $g_{\text{GJ}} = 666$ mS/cm^{-2}, $R_{\text{c}} = 0$, and $\Delta x_{\text{micro}} = 2.5 \cdot 10^{-2}$ cm. The multiscale models agree quite well with their corresponding microscale analogues for all sampled values of Δx_{macro}

5 Discussion and Conclusion

The intentions of this article are twofold: (1) to provide a modified version of the adaptive multiscale model of Hand and Griffith (2010) that will better generalize to three spatial dimensions, and (2) to demonstrate empirically that this multiscale model captures both the activation and recovery dynamics of its corresponding purely microscale representation. The primary differences between the present model and that of Hand and Griffith (2010) are in the interface conditions and the arrangement of myocytes with respect to the macroscopically imposed grid. Secondary differences include the ionic model and the adaptivity criteria. We empirically study the effects of macroscale grid spacing on wavespeed and waveform for a variety of parameter regimes. For a thorough analysis of the accuracy of the adaptive multiscale method as a function of g_{GJ} and for a detailed comparison of the adaptive multiscale model to its fully macroscale counterpart, see Hand and Griffith (2010). Note, however, that unlike the present article, Hand and Griffith (2010) did not consider the repolarization dynamics or the case of purely ephaptic conduction. Nonetheless, we note that the present model and that of Hand and Griffith (2010) have comparable accuracy and computational cost. As the primary limita-

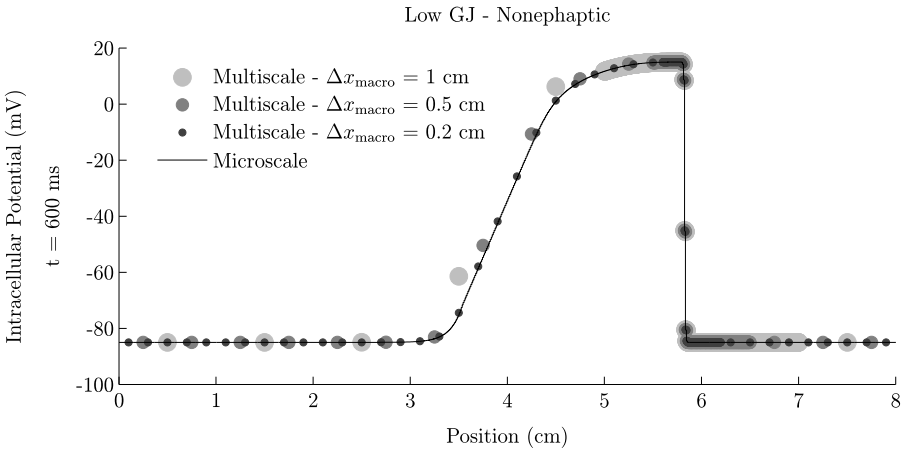

Fig. 4 The intracellular potential at a single time for the low gap-junctional, nonephaptic simulations with varying macroscale grid spacing. Note that myocytes are resolved only near the upstroke. While the upstroke is only about four cells wide, it is resolved by about 24 nodes, as each cell contains 6 grid points. In these simulations, $g_{\text{GJ}} = 6.66$ mS/cm^{-2}, $R_{\text{c}} = 0$, and $\Delta x_{\text{micro}} = 2.5 \cdot 10^{-2}$ cm. There is visible quantitative disagreement between the multiscale and microscale models only for $\Delta x_{\text{macro}} = 0.5$ or 1 cm, each a sizable fraction of the length scale of the action potential

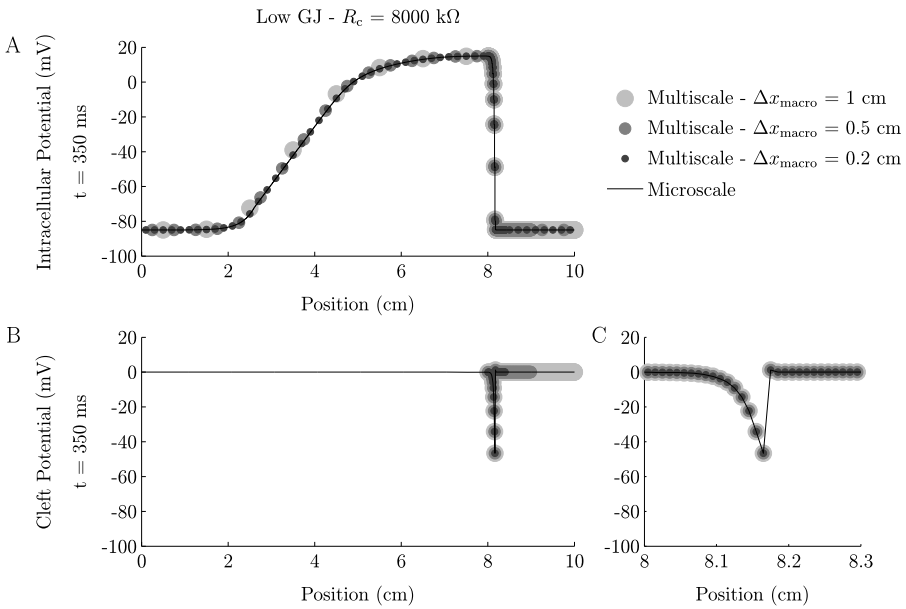

Fig. 5 The intracellular (**A**) and cleft (**B**, **C**) potential at a single time for the low gap-junctional, ephaptic simulations with varying macroscale grid spacing. Because cleft potentials in the low-resolution regions are not explicitly modeled, panel **B** does not present them from multiscale simulations in those regions. Panel **C** provides a magnification of panel **B** near the action potential upstroke. Panels **A** and **B** show that myocytes are resolved only near the upstroke. In these simulations, $g_{\text{GJ}} = 6.66$ mS/cm^{-2}, $R_{\text{c}} = 8000$ kΩ, and $\Delta x_{\text{micro}} = 2.5 \cdot 10^{-2}$ cm. There is visible quantitative disagreement between the multiscale and microscale models only for $\Delta x_{\text{macro}} = 1$ cm, a sizable fraction of the length scale of the action potential

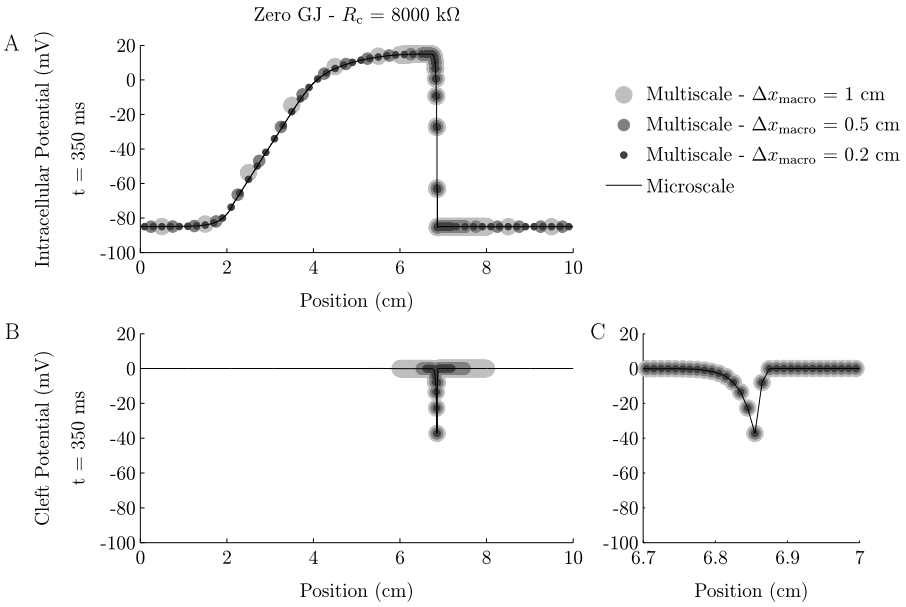

Fig. 6 The intracellular (**A**) and cleft (**B**) potential at a single time for the zero gap-junctional, ephaptic simulations with varying macroscale grid spacing. Because cleft potentials in the low-resolution regions are not explicitly modeled, panel **B** does not present cleft potentials from multiscale simulations in those regions. Panel **C** provides a magnification of panel **B** near the action potential upstroke. Panels **A** and **B** show that myocytes are resolved only near the upstroke. In these simulations, $g_{GJ} = 0$, $R_c = 8000\,\text{k}\Omega$, and $\Delta x_{micro} = 2.5 \cdot 10^{-2}$ cm. There is visible quantitative disagreement between the multiscale and microscale models only for $\Delta x_{macro} = 1$ cm, a sizable fraction of the length scale of the action potential

tion of the present model is its one-dimensionality, we emphasize throughout this section the implications and challenges of two- and three-dimensional generalizations.

Our primary conclusion is that the modified one-dimensional multiscale method accurately captures action potential wavespeeds and waveforms over a wide range of gap-junctional coupling levels. Further, this conclusion holds in the presence or absence of an ephaptic coupling effect, including in the purely ephaptic regime in which the model includes no gap-junctional coupling. We thus have replicated the work of Hand and Griffith (2010) using different interface conditions, adaptivity criteria, and ionic models. Moreover, we have extended these earlier results to demonstrate that recovery is also accurately captured by the adaptive multiscale model, provided that macroscale grid spacing is not too large relative to the spatial extent of the traveling action potential. We remark that the waveforms of cleft potential are also accurately recovered, even though they are only nonzero in the highly resolved regions. Thus, this empirical study justifies the assumption that cleft potential can be ignored away from wavefronts.

A second conclusion is that coincident boundaries of microscale myocytes and the macroscale grid are not required by our multiscale method. This observation is vital because realistic two- and three-dimensional simulations will have deformation,

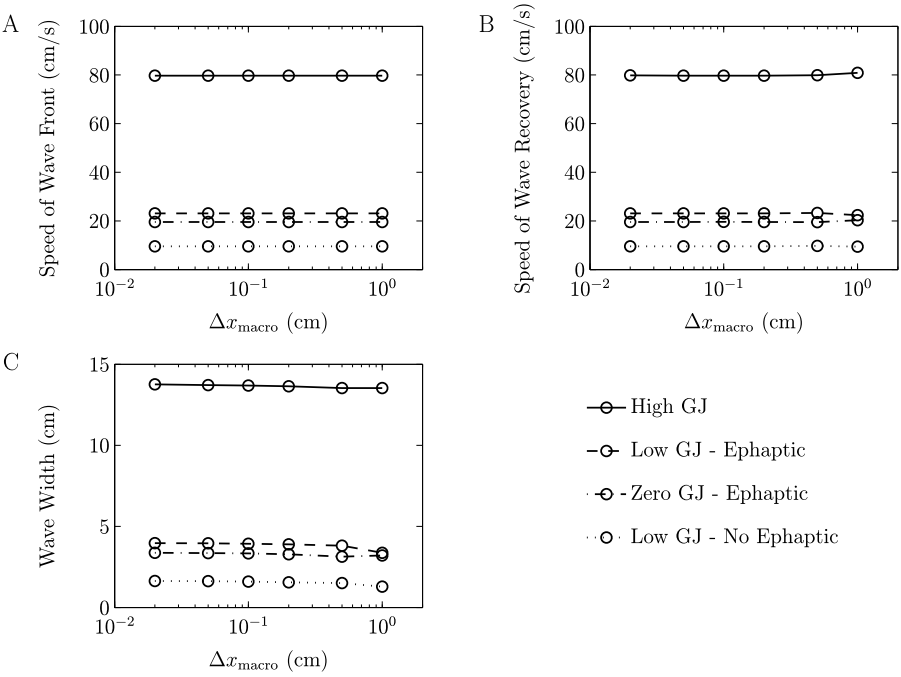

Fig. 7 Plots of wavespeed at upstroke (**A**), wavespeed at recovery (**B**), and wavewidth (**C**) for multiscale simulations as a function of macroscale grid spacing. Each line is based on 6 simulations, depicted by circles, for roughly logarithmically spaced values of Δx_{macro}. There is little dependence of any of these variables on Δx_{macro} over the values surveyed

offset, and skewing of myocytes relative to any macroscopically imposed grid. The most important feature of our model for this observation is the interface conditions between the macroscale and the microscale. As mentioned in Sect. 2.3, the new interface conditions do not focus on gap-junctional current, which only exists at the ends of cells. Instead, they equate cytosolic potential and current, which exist throughout the entire cell body. In particular, even if the end of a myocyte occurs at the boundary of the high-resolution region, the cytosolic potential and current at the cell's end are well defined, and the interface conditions can be implemented as written. Additionally, these less restrictive assumptions on myocyte geometry will facilitate studying tissues with heterogeneity in cell length.

Much research is still needed to exploit the flexibility of microscale and macroscale gridding in several dimensions. Specifically, simulations are needed to determine the best way of describing resolved myocytes in two or three spatial dimensions. For example, myocytes could be considered as genuinely two- or three-dimensional domains over which Laplace's equation is solved. Alternatively, they could be considered as coupled one-dimensional domains over which cable equations are solved. In either case, the microscale grid would be locally aligned with the microscale cells, but it need not be aligned with the macroscopically imposed grid. See Hand and Griffith (2010) for a more complete description of these two possibilities.

A third conclusion of this study is that macroscale grid spacing can be extremely coarse without introducing significant errors in one-dimensional conduction speeds or waveforms. The accuracy of the coarsest simulations in Figs. 3–7 suggests that Δx_{macro} can be chosen simply to ensure that there are approximately ten macroscopic nodes across the entire action potential, regardless of the spatial extent of the action potential upstroke. As a result, it may be possible to use a grid spacing of 0.1–1 cm away from the upstroke. In contrast, fully-macroscale simulations must resolve the upstroke, but they cannot use such coarse values of Δx_{macro} in a uniform fashion. We do not provide detailed timing results for our simulations because such results are highly dependent on dimension and domain size. Even in one dimension, the apparent gain in computational speed could be made quite large by choosing a long enough domain.

Further simulations are needed to determine whether such large macroscale spacings would yield acceptable accuracy in two- or three-dimensional models. If they do, the computational burden of whole-heart simulations could be greatly reduced. Currently, many such simulations use grid spacings around 100–250 μm in the tissue bulk (Colli Franzone et al. 2006; Bordas et al. 2009; Keldermann et al. 2009). In three spatial dimensions, this could correspond to a computational savings of many orders of magnitude.

Another important development needed to generalize the current work to more realistic settings is the inclusion of a bidomain formulation. As part of this formulation, the cleft would need to be coupled to the extracellular space, possibly through a point current injection. Such simulations may need to preferentially resolve extracellular space around clefts. Alternatively, they may be able to have extracellular resolution much less than intracellular resolution. For work developing a purely-microscale version of such a generalization, see Lin and Keener (2010).

One limitation of the present study is the lack of a detailed, realistic ionic current model. For example, the Fenton–Karma simplification does not explicitly describe intracellular Ca^{2+} release. The present modeling framework may be generalized to treat cellular models that include detailed descriptions of intracellular ion dynamics, such as in Luo and Rudy (1994). At the microscale level, such details could be included in either a distributed manner, by tracking one set of intracellular variables per myocyte, or in a more detailed manner, by tracking one set of intracellular variables per microscale node. At the macroscale level, such details would be tracked in a spatially averaged sense. Conservative restriction and prolongation procedures would be used to transfer intracellular variables between macroscale and microscale representations, as is currently done with the potential and gating variables. Such simulations may even require higher resolution around regions away from the action potential upstroke. In such a case the adaptivity condition would need to be modified to select the new features of interest. In all of these scenarios, the modifications will likely be highly dependent on the particular model and application. The specific constants may change in accordance with upstroke speed and conduction velocity, but we expect that adaptivity criteria will remain qualitatively similar to (12)–(13). In any case, the interface conditions, (10)–(11), would hold as written.

As described in this paper, and as visible in Figs. 3–6, larger values of Δx_{macro} cause a much larger number of cells to be included in the high-resolution regions near action potential upstrokes. Such large regions of resolved myocytes could be quite computationally expensive and even unnecessary if, for example, the wavefront is significantly smaller than Δx_{macro}. In such a case, it may be useful to combine the multiscale model adaptivity approach of this work with a more traditional macroscale mesh adaptivity approach, in which the macroscale region of the computational domain would be described using an adaptively refined computational grid (Cherry et al. 2000, 2003; Colli Franzone et al. 2006). We leave a detailed investigation of this possibility as future work.

Acknowledgements We are indebted to Glenn Fishman and Charles Peskin for helpful discussions. This work was supported in part by a Whitehead Foundation Junior Faculty Fellowship awarded to Boyce Griffith.

Appendix A: Numerical Discretization

A.1 Spatial Discretization

Let V_i be the intracellular potential of the ith macroscale node, and let $v_{j,k}$ be the intracellular potential of the kth node within the jth resolved myocyte, with $k = 1, \ldots, n$. Let $v_{j,1/2}$ and $v_{j,n+1/2}$ represent the potential at the left and right ends of the jth myocyte, respectively. For convenience, we introduce ghost values $v_{j,0} := 2v_{j,1/2} - v_{j,1}$ and $v_{j,n+1} := 2v_{j,n+1/2} - v_{j,n}$. Similarly, let W_i be the gating variables at the ith macroscale node, and let $w_{j,k}$ be the gating variables for the kth node of the jth cell.

The semi-discretized microscale system is:

$$C\frac{\mathrm{d}}{\mathrm{d}t}v_{j,k} = \frac{A\sigma_{\text{cyt}}}{S}\frac{v_{j,k-1} - 2v_{j,k} + v_{j,k+1}}{\Delta x_{\text{micro}}^2} - I_{\text{ion,side}}(v_{j,k}, w_{j,k}) \quad \text{for } 1 \le k \le n, \tag{16}$$

$$C\frac{\mathrm{d}}{\mathrm{d}t}(v_{j,1/2} - v_{\text{c},j-1}) = \sigma_{\text{cyt}}\frac{v_{j,1} - v_{j,1/2}}{\Delta x_{\text{micro}}/2} - g_{\text{GJ}}(v_{j,1/2} - v_{j-1,n+1/2}) - I_{\text{ion,end}}(v_{j,1/2} - v_{\text{c},j-1}, w_{j,1/2}), \tag{17}$$

$$C\frac{\mathrm{d}}{\mathrm{d}t}(v_{j,n+1/2} - v_{\text{c},j}) = \sigma_{\text{cyt}}\frac{v_{i,j}n - v_{j,n+1/2}}{\Delta x_{\text{micro}}/2} - g_{\text{GJ}}(v_{j,n+1/2} - v_{j+1,1/2}) - I_{\text{ion,end}}(v_{j,n+1/2} - v_{\text{c},j}, w_{j,n+1/2}), \tag{18}$$

$$\frac{\mathrm{d}}{\mathrm{d}t} w_{j,k} = g(v_{j,k}, w_{j,k}) \quad \text{for } 1 \le k \le n, \tag{19}$$

$$\frac{\mathrm{d}}{\mathrm{d}t} w_{j,1/2} = g(v_{j,1/2} - v_{\mathrm{c},j-1}, w_{j,1/2}), \tag{20}$$

$$\frac{\mathrm{d}}{\mathrm{d}t} w_{j,n+1/2} = g(v_{j,n+1/2} - v_{\mathrm{c},j}, w_{j,n+1/2}), \tag{21}$$

$$v_{\mathrm{c},j} = \begin{cases} \sigma_{\mathrm{cyt}} R_{\mathrm{c}} A \left(\frac{v_{j,n} - v_{j,n+1/2}}{\Delta x_{\mathrm{micro}}/2} + \frac{v_{j+1,1} - v_{j+1,1/2}}{\Delta x_{\mathrm{micro}}/2} \right), & \text{or} \\ 0, \end{cases} \tag{22}$$

in which the top entry of the braces in (22) is used only if both biological cells adjacent to the jth cleft are resolved. Equations (16)–(18) are second-order accurate finite-volume discretizations of the PDE and boundary conditions (1)–(3).

The semi-discretized macroscale system is:

$$C \frac{\mathrm{d}}{\mathrm{d}t} V_i = \frac{1}{S\ell + 2A} \frac{\ell}{\Delta x_{\mathrm{macro}}} \left(A \sigma_{\mathrm{cyt}} \left(1 - \frac{1}{1+\kappa} \right) \frac{V_{i-1} - 2V_i + V_{i+1}}{\Delta x_{\mathrm{macro}}} \right) - I_{\mathrm{ion}}(V_i, W_i), \tag{23}$$

$$\frac{\mathrm{d}}{\mathrm{d}t} W_i = g(V_i, W_i). \tag{24}$$

This system is a second-order accurate finite-volume discretization of (8)–(9).

The interface conditions can be discretized to second order by introducing values at two additional ghost nodes, one at the macroscale and one at the microscale. Let i^* be the index of the low-resolution macroscale volume adjacent to the interface. Let j^* be the index of the resolved myocyte immediately adjacent to the interface. Let k^* be the index of the first resolved node within that myocyte. Note that $k^* = 1$ if the coarse-fine interface coincides with the cell's left end and $k^* > 1$ if the interface intersects the coarse-fine interface within the cell interior. For concreteness, we assume that the high-resolution region is on the right side of the coarse-fine interface. We introduce the ghost values $\widehat{V_{i^*+1}}$ and $\widehat{v_{j^*,k^*-1}}$, and we discretize (10)–(11) as

$$\frac{\widehat{V_{i^*+1}} + V_{i^*}}{2} = \frac{v_{j^*,k^*} + \widehat{v_{j^*,k^*-1}}}{2}, \tag{25}$$

$$-\left(1 - \frac{1}{1+\kappa} \right) \frac{\widehat{V_{i^*+1}} - V_{i^*}}{\Delta x_{\mathrm{macro}}} = -\frac{v_{j^*,k^*} - \widehat{v_{j^*,k^*-1}}}{\Delta x_{\mathrm{micro}}}, \tag{26}$$

respectively. The ghost values $\widehat{V_{i^*+1}}$ and $\widehat{v_{j^*,k^*-1}}$ are substituted for V_{i^*+1} and v_{j^*,k^*-1} in (16) and (23). Analogous equations hold at a coarse-fine interface for which the high-resolution region is to the left of the low-resolution region.

A.2 Temporal Discretization

A difficulty in numerically simulating (16)–(26) is that the second-order spatial derivatives in (16) and (23) result in severe timestep size restrictions if treated explicitly, whereas the nonlinear ionic current terms are generally difficult to treat implicitly. Hence, we use a second-order accurate Strang operator splitting. For a fixed multiscale grid, we write our semi-discretized PDE system (16)–(26) in the form

$$\frac{\mathrm{d}}{\mathrm{d}t} L_{\mathrm{trans}} \mathcal{V} = L_{\mathrm{imp}} \mathcal{V} + f_{\mathrm{exp}}(\mathcal{V}, \mathcal{W}), \tag{27}$$

$$\frac{\mathrm{d}}{\mathrm{d}t} \mathcal{W} = g(L_{\mathrm{trans}} \mathcal{V}, \mathcal{W}), \tag{28}$$

in which $\mathcal{V}$ is a column vector of the microscale and macroscale potentials, and $\mathcal{W}$ is a column vector of the microscale and macroscale gating variables. L_{trans} is a matrix whose action on $\mathcal{V}$ returns the transmembrane potential of each node. Specifically, it returns the cleft potential for interior nodes, and it returns the difference of the intracellular potential from the cleft potential for boundary nodes. Note that L_{trans} is generally not a diagonal matrix. Thus, even if we were to treat (27)–(28) explicitly, we would still need to solve a system of linear equations at each timestep. L_{imp} is a matrix that contains the nonionic terms related to gap-junctional and ephaptic coupling, terms that are linear in $\mathcal{V}$, and f_{exp} is a nonlinear function of $\mathcal{V}$ and $\mathcal{W}$ that contains only terms related to the transmembrane ionic current.

To determine the values of $\mathcal{V}$ and $\mathcal{W}$ at time $t + \Delta t$ given their values at time t, we perform the following computations: First, we evolve

$$\frac{\mathrm{d}}{\mathrm{d}t} L_{\mathrm{trans}} \mathcal{V} = f_{\mathrm{exp}}(\mathcal{V}, \mathcal{W}), \tag{29}$$

$$\frac{\mathrm{d}}{\mathrm{d}t} \mathcal{W} = g(L_{\mathrm{trans}} \mathcal{V}, \mathcal{W}), \tag{30}$$

over the time interval $\Delta t/2$ using a second-order accurate, two-stage, explicit Runge–Kutta method. Because L_{trans} is not generally a diagonal matrix, this explicit solution method generally requires the solution of a sparse linear system of equations. Then, we evolve

$$\frac{\mathrm{d}}{\mathrm{d}t} L_{\mathrm{trans}} \mathcal{V} = L_{\mathrm{imp}} \mathcal{V}, \tag{31}$$

$$\frac{\mathrm{d}}{\mathrm{d}t} \mathcal{W} = 0, \tag{32}$$

over the time interval Δt using a second-order accurate Crank–Nicolson scheme. We remark again that L_{trans} is not generally a diagonal matrix. Consequently, even if we were to treat (31) explicitly, we would still need to solve a sparse system of linear equations when solving (31)–(32) during each timestep.

Finally, we evolve (29)–(30) again over the interval $\Delta t/2$. The overall scheme is second-order accurate in time.

Appendix B: Parameters

Table 1 Table of the measurable and derived parameters that enter our adaptive macroscale simulations. For ephaptic models, the cleft width is $w_{\text{cleft}} = 7$ nm. Otherwise, for nonephaptic models, $R_c = 0$ and $\phi_c = 0$ mV, which correspond to a very large cleft width

Measurable Parameters

Symbol	Parameter	Value	Reference
r	radius of cell	$11 \cdot 10^{-4}$ cm	(Kucera et al. 2002)
ℓ	length of cell	10^{-2} cm	(Kucera et al. 2002)
σ_{cyt}	cytosolic conductivity	6.67 mS cm^{-1}	(Kucera et al. 2002)
σ_{ext}	extracellular conductivity	6.67 mS cm^{-1}	(Kucera et al. 2002)
g_{GJ}	gap-junctional conductance per area	0–$6.66 \cdot 10^{2}$ mS cm^{-2}	(Kucera et al. 2002)
C	membrane capacitance per area	1 μF cm^{-2}	(Kucera et al. 2002)

Derived Parameters

Symbol	Parameter	Expression
A	area of cross-section	πr^2
S	circumference of cross-section	$2\pi r$
κ	nondimensional gap-junctional conductivity	$\ell g_{\text{GJ}}/\sigma_{\text{cyt}}$
R_c	cleft-to-ground resistance	$1/8\pi\sigma_{\text{ext}} w_{\text{cleft}}$

References

Bordas, R., Carpentieri, B., Fotia, G., Maggio, F., Nobes, R., Pitt-Francis, J., & Southern, J. (2009). Simulation of cardiac electrophysiology on next-generation high-performance computers. *Philos. Trans. R. Soc. A*, *367*, 1951–1969.

Boron, W., & Boulpaep, E. (2005). *Medical physiology*. Philadelphia: Saunders.

Cherry, E., Greenside, H., & Henriquez, C. (2000). A space-time adaptive method for simulating complex cardiac dynamics. *Phys. Rev. Lett.*, *84*, 1343–1346.

Cherry, E., Greenside, H., & Henriquez, C. (2003). Efficient simulation of three-dimensional anisotropic cardiac tissue using an adaptive mesh refinement method. *Chaos*, *13*, 853–865.

Colli Franzone, P., Deuflhard, P., Erdmann, B., Lang, J., & Pavarino, L. (2006). Adaptivity in space and time for reaction-diffusion systems in electrocardiology. *SIAM J. Sci. Comput.*, *28*, 942–962.

Copene, E., & Keener, J. (2008). Ephaptic coupling of cardiac cells through the junctional electric potential. *J. Math. Biol.*, *57*, 265–284.

Fenton, F., & Karma, A. (1998). Vortex dynamics in three-dimensional continuous myocardium with fiber rotation: Filament instability and fibrillation. *Chaos*, *8*, 20–47.

Gutstein, D., Morley, G., Tamaddon, H., Vaidya, D., Schneider, M., Chen, J., Chien, K., Stuhlmann, H., & Fishman, G. (2001). Conduction slowing and sudden arrhythmic death in mice with cardiac-restricted inactivation of connexin43. *Circ. Res.*, *88*, 333–339.

Hand, P., & Griffith, B. (2010). Adaptive multiscale model for simulating cardiac conduction. *Proc. Natl. Acad. Sci. USA*, *107*(33), 14603–14608.

Hand, P., & Peskin, C. (2010). Homogenization of an electrophysiological model for a strand of cardiac myocytes with gap-junctional and electric-field coupling. *Bull. Math. Biol.*, *72*, 1408–1424.

Hand, P., Griffith, B., & Peskin, C. (2009). Deriving macroscopic myocardial conductivities by homogenization of microscopic models. *Bull. Math. Biol.*, *71*, 1707–1726.

Keener, J., & Sneyd, J. (1998). *Mathematical physiology*. Berlin: Springer.
Keldermann, R., ten Tusscher, K., Nash, M., Bradley, C., Hren, R., Taggart, P., & Panfilov, A. (2009). A computational study of mother rotor VF in the human ventricles. *Am. J. Physiol., Heart Circ. Physiol.*, *296*(2), H370–H379.
Kucera, J., Rohr, S., & Rudy, Y. (2002). Localization of sodium channels in intercalated disks modulates cardiac conduction. *Circ. Res.*, *91*, 1176–1182.
Lin, J., & Keener, J. (2010). Modeling electrical activity of myocardial cells incorporating the effects of ephaptic coupling. *Proc. Natl. Acad. Sci. USA*, *107*(49), 20935–20940.
Luo, C., & Rudy, Y. (1994). A dynamic model of the cardiac ventricular action potential. I. Simulations of ionic currents and concentration changes. *Circ. Res.*, *74*(6), 1071–1096.
Mori, Y., Fishman, G., & Peskin, C. (2008). Ephaptic conduction in a cardiac strand model with 3d electrodiffusion. *Proc. Natl. Acad. Sci. USA*, *105*, 6463–6468.
Neu, J., & Krassowska, W. (1993). Homogenization of syncytial tissues. *Crit. Rev. Biomed. Eng.*, *21*, 137–199.
Peters, N., Green, C., Poole-Wilson, P., & Severs, N. (1993). Reduced content of connexin43 gap junctions in ventricular myocardium from hypertrophied and ischemic human hearts. *Circulation*, *88*(3), 864–875.
Picone, J., Sperelakis, N., & Mann, J. (1991). Expanded model of the electric field hypothesis for propagation in cardiac muscle. *Math. Comput. Model.*, *15*, 13–35.
Ramasamy, L., & Sperelakis, N. (2007). Cable properties and propagation velocity in a long single chain of simulated myocardial cells. *Theor. Biol. Med. Model.*, *4*, 36.
Rohr, S. (2004). Role of gap junctions in the propagation of the cardiac action potential. *Cardiovasc. Res.*, *62*, 309–322.
Severs, N., Coppen, S., Dupont, E., Yeh, H., Ko, Y., & Matsushita, T. (2004). Gap junction alterations in human cardiac disease. *Cardiovasc. Res.*, *62*(2), 368–377.
Severs, N., Bruce, A., Dupont, E., & Rothery, S. (2008). Remodelling of gap junctions and connexin expression in diseased myocardium. *Cardiovasc. Res.*, *80*(1), 9–19.
Smith, J., Green, C., Peters, N., Rothery, S., & Severs, N. J. (1991). Altered patterns of gap junction distribution in ischemic heart disease. An immunohistochemical study of human myocardium using laser scanning confocal microscopy. *Am. J. Pathol.*, *139*(4), 801–821.
Sperelakis, N., & Mann, J. (1977). Evaluation of electric field changes in the cleft between excitable cells. *J. Theor. Biol.*, *64*, 71–96.
Yao, J., Gutstein, D., Liu, F., Fishman, G., & Wit, A. (2003). Cell coupling between ventricular myocyte pairs from connexin43-deficient murine hearts. *Circ. Res.*, *93*(8), 736–743.